Observation of Jumping Cirrus with Ground-Based Cameras, Radiosonde, and Himawari-8

Takafumi SEGUCHI, Suginori IWASAKI

Department of Earth and Ocean Sciences, National Defense Academy, Kanagawa, Japan

Masashi KAMOGAWA[1]

Department of Physics, Tokyo Gakugei University, Tokyo, Japan

Tomoki USHIYAMA

International Centre for Water Hazard and Risk Management, Public Works Research Institute, Tsukuba, Japan

and

Hajime OKAMOTO

Research Institute for Applied Mechanics, Kyushu University, Fukuoka, Japan

(Manuscript received 12 October 2018, in final form 22 January 2019)

Abstract

In the summer of 2016, 14 cases of jumping cirrus (JC) were observed around the Kanto region in Japan by ground-based, visible-light cameras. The cameras were set at the summit of Mt. Fuji and National Defense Academy (Kanagawa, Japan), and 15-second time-lapse photography was continually taken for the period. The location and spatial scale of the JC were calculated by measurements using the photometry of background stars in the nighttime and the geostationary meteorological satellite Himawari-8 infrared imagery. The environmental conditions of the JC were also investigated using radiosonde and Himawari-8 visible and infrared measurements. Comparing our cases to the JC in the United States of America (USA) reproduced by a three-dimensional, non-hydrostatic cloud model from previous studies, their motions, morphology, spatial and temporal scales showed similarities, although the horizontal scale of the JC and the magnitude of the underlying convection was relatively smaller in our cases. The sounding by the radiosonde in the vicinity of the storms showed that 3 of the 14 cases reached the stratosphere. However, the hydration of the lower stratosphere was not supported by analysis of the brightness temperature difference (BTD) between 6.2 and 10.4 μm measured by Himawari-8. The averaged wind shear across the range of the jumping heights above the anvil was −1.1 m s^{-1} km^{-1}. The maximum value of the convective available potential energy (CAPE) of the 14 cases was 1384 J kg^{-1}, which is several times smaller than those of the thunderstorm cases observed in the USA in previous numerical JC studies. This indicates that JC occurs from the cumulonimbus anvil top even if the convection is relatively weak. The motion of JC observed

Corresponding author: Iwasaki Suginori, Department of Earth and Ocean Sciences, National Defense Academy, 1-10-20, Hashirimizu, Yokosuka, Kanagawa 239-8686, Japan
E-mail: iwasaki@nda.ac.jp
1 Present affiliation: Global Center for Asian and Regional Research, University of Shizuoka, Shizuoka, Shizuoka 420-0839, Japan
J-stage Advance Published Date: 4 February 2019

by visible-light cameras shows that it can transport moisture above the tops of the anvils of convective clouds regardless of its altitude as cloud ice appears to be sublimated.

Keywords jumping cirrus; ground-based camera observation; convective cloud; overshooting top; above-anvil cirrus plume

Citation Seguchi, T., S. Iwasaki, M. Kamogawa, T. Ushiyama, and H. Okamoto, 2019: Observation of jumping cirrus with ground-based cameras, radiosonde, and Himawari-8. *J. Meteor. Soc. Japan*, **97**, 615–632, doi:10.2151/jmsj.2019-033.

1. Introduction

Water vapor in the stratosphere impacts the global climate system. Solomon et al. (2010) demonstrated that the decadal change of the stratospheric water vapor concentration influences the rate of global warming. Thus, it is crucial to understand the origins of stratospheric water vapor.

Some studies have focused on the rapid injection of water vapor into the lower stratosphere (LS) via cloud protrusions by tropospheric deep convective storms. In earlier research, the overshooting phenomena at the cloud top were mainly studied as a possible mechanism of the rapid transportation of water vapor into the LS. Danielsen (1993) found overshooting turrets that penetrated deep enough to enter the tropical LS by the irreversible mass transportation with in situ observation. Nielsen et al. (2007) also found solid particles in the tropical lowest stratosphere, 200 km distant from deep convective events. These may be evidence of the transportation of water and other substances into the stratosphere by deep convection. Iwasaki et al. (2010) indicated that one event of overshooting top (OT) could lift 100 tons of water into the LS. However, if the OT is an adiabatic phenomenon, the water sinks back into the troposphere instantly afterward and thus cannot hydrate the stratosphere.

As a diabatic mechanism of the cross-tropopause transport of water vapor, a type of cirrus cloud named "jumping cirrus (JC)", caused by collapses of the OTs, has been recorded by various ground and aircraft observations in the midlatitudes. In an older study, Fujita (1974) discovered a stratospheric cirrus cloud jumping up and extending above the anvil of severe thunderstorms during an aircraft observation project focused on overshooting phenomena. In his later work, he reviewed those observations and mentioned the JC again, saying, "one of the most striking features seen repeatedly above the anvil top is the formation of the cirrus cloud which jumps upward from behind the overshooting dome as it collapses violently into anvil cloud" (Fujita 1982). This may be how the term "jumping" cirrus came into usage.

Unlike OTs, JC appears to partly evaporate above anvil top, whereas some of its cloud particles sink back to the anvil. Accordingly, if a storm is sufficiently strong and thus the anvil top reaches the tropopause, JC has a potential to moisten the LS. They are thought to be the morphological and visual evidence of the transportation of water from the upper troposphere (UT) to the LS.

Associated with the OT and the JC, the existence of broadly extending plume-like cirrus cloud above the anvil top, known as above-anvil cirrus plume (AACP), has also been revealed by aircraft observations (Fujita 1974, 1982) and satellites (Setvák and Doswell 1991). This AACP, a type of stratospheric cirrus cloud, is another likely evidence of the stratospheric water vapor generated by tropospheric thunderstorms. The AACP can be detected by the satellite's visible-light and infrared (IR) imagery as it typically casts a shadow on the underlying anvil and its temperature is usually warmer than that of the underlying anvil top due to its adjustment to the ambient warm air in the LS. Presently, there are more mechanisms discussed as responsible for the AACP formation. One of those is multiple injections of water vapor by the JC which enters the LS (Wang et al. 2011; Homeyer et al. 2017).

Bedka et al. (2018) detected AACPs with the Geostationary Operational Environmental Satellite (GOES) and inspected the relevance of weather severity and AACP formation by examining ground-based Doppler radars, observations of lightning, and severe weather reports. They claim that the AACP is usually created by intense deep convection with a high cloud top, strong updraft, and significant lightning. Therefore, AACPs can be useful for weather forecasting as they can serve as one of the indicators of severe weather, with a lead time up to 30 minutes.

In this paper, we focus on the JC only, distinguish-

ing it strictly from the AACP. When we refer to the JC, the jumping process from the anvil top must be unambiguously observed. Even if the AACP was detected, it is not sufficient evidence of the existence of JC; although some discussions are implying the relevance between JC and AACPs (Wang et al. 2011; Homeyer et al. 2017).

Further studies (mentioned below) have revealed various aspects of the relationship between deep convection, JC, and AACPs by utilizing numerical cloud model simulations, simultaneous satellites, radar networks, and in situ observations.

Wang (2003, 2004) and Wang et al. (2011) used a three-dimensional, non-hydrostatic cloud model to show that the JC seemed to occur diabatically by the gravity wave breaking excited by the collapse of OTs, protrude ~ 1–2 km above the anvil cloud of a large cumulonimbus at the vertical speed of ~ 10 m s^{-1}, and reach an altitude of ~ 15 km with a horizontal scale of ~ 5–15 km in about 10 minutes (Fig. 7 by Wang et al. 2011).

According to their research, the JC is assumed to occur in the following order. (1) Convective storms develop, and the anvil spreads at the altitude where buoyancy becomes neutral. (2) Strong updraft creates an OT, which begins to sink after it loses its energy shortly afterward. (3) JC is caused by the breaking of a gravity wave generated by the collapse of this OT (Fig. 1). In our study, this concept serves as criteria used to detect JC cases in our camera observations.

Sang et al. (2018) used a cloud-resolving large eddy model to demonstrate that the overshooting convection moistened the LS due to the gravity wave breaking and ice sublimation near the tropopause. They suggest that the vertical wind shear near tropopause affects the gravity wave breaking as opposed to the overshooting.

Hassim and Lane (2010) used the weather research and forecasting model to demonstrate that the JC also occurs in the tropical tropopause layer (TTL) and moistens the TTL, induced by the collapse of the overshooting turret and the resulting TTL mixing.

In addition to the progress of model research, observations of real cases have also been conducted—though they pose a big challenge. In situ observation by aircraft, as a method for measuring local atmospheric conditions and recording changes in JC's appearance (motion), would be extremely dangerous due to the severity of deep convective storms and related near-cloud-top turbulence. Furthermore, it is difficult to cover a wide observation area solely by a single aircraft.

The imagery from meteorological satellites, such as the advanced very high-resolution radiometer (Setvák and Doswell 1991; Levizzani and Setvák 1996), the moderate resolution imaging spectroradiometer (Wang et al. 2009) (both are aboard the polar orbiting satellites), and the GOES (Bedka et al. 2018), are used to obtain an overview of the horizontal cross-section of top of deep convective storms. However, unlike AACPs, JC is too thin to be seen by the satellites' imagers and distinguished from the underlying extensive anvil, though its horizontal scale is assumed to be approximately 10–15 km and enough to overcome the matter of spatial resolution. Additionally, the vertical information of JC cannot be obtained by satellite imagers.

In addition to imagers, other space-borne instruments are also used to investigate atmospheric conditions. Figure 9a by Wang et al. (2011) highlights a case where the cloud profiling radar aboard the CloudSat was able to observe the vertical structure of JC. However, because the CALIOP and CloudSat are polar orbiting satellites, they do not possess adequate temporal resolution, and thus we cannot observe the consecutive change of JC. Setvák et al. (2008) showed that the air above severe thunderstorms was moistened using the brightness temperature difference (BTD) value (Schmetz et al. 1997). In these studies, the BTD was calculated by subtracting the black body temperature (T_{bb}) of the IR band (10.8 μm) from that of the water vapor absorption band (6.2 μm) of the Meteosat Second Generation Spinning Enhanced Visible and Infrared Imager. If water vapor exists in the LS where the air temperature is warmer than in the UT, at the anvil top layer, the T_{bb} of the water vapor absorption band is higher than that of the cloud top, and thus, the BTD value is positive.

As mentioned above, various methods have been employed to analyze JC. Because of the matters of currently available instruments, JC is rarely observed, and we do not know much about JC, except for its spatial and temporal scale mainly based on the model studies. However, JC is likely to be a ubiquitous and frequent phenomenon to deep convective storms and thus has a potential to impact the stratospheric water vapor budget. Wang (2003) estimated that the rapid cross-tropopause transportation of water vapor triggered by the JC with one typical deep convective storm cell is 3 tons s^{-1} and globally about half a billion tons per day. Previous studies lack more observation-oriented analyses to support the inferences from the model studies. The ground-based observation has an advantage of low cost, and it can observe the consecutive change of horizontal and vertical development of

the cloud for a long period, but quantitative analyses, such as calculation of JC's size, lifetime, and speed, from ground-based observation have never been examined.

In this study, we focused on observing JC using ground-based visible-light cameras and investigated their characteristics such as motion and morphology. We then conducted quantitative analyses of the spatial and temporal scale of the JC. At the same time, using data from a radiosonde, the geostationary meteorological satellite Himawari-8, and a ground precipitation radar, we analyzed the environmental conditions around the convective storms where the JC occur to clarify the features specific to the JC and the underlying convective storms. In particular, we paid significant attention to the characteristics of the JC specific to the local area by comparing the results with previous studies.

Section 2 describes the instruments and data used in our study and explains the observation method and criteria used to detect the JC. Section 3 demonstrates how the detected JC was analyzed using Himawari-8, a ground precipitation radar, and radiosonde data, focusing on a specific case. Then, in Section 4 summarizing the results from all of the cases, the JC's characteristics are discussed. Finally, the averaged values and features of all 14 JC cases are summarized in Section 5.

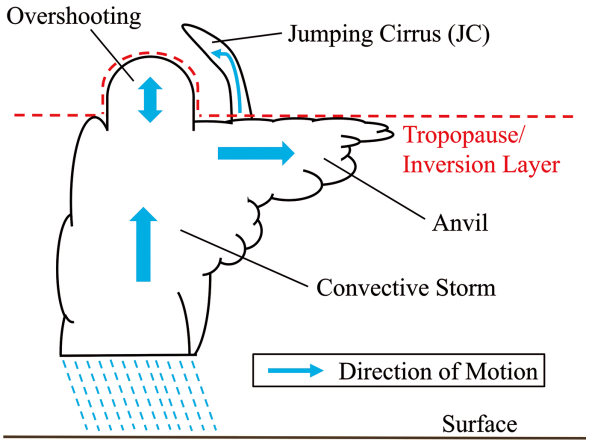

Fig. 1. Schematic diagram of apparent features of jumping cirrus (JC). The blue arrows denote the direction of motion of the cloud particles. They indicate that air lifted from the ground grows into a convective storm, extends laterally, and forms anvil clouds. The double arrow describes the motion of an OT that ascends and sinks atop the convective storm. The broken red line denotes the altitude where the tropopause or the inversion layer lies—note that the anvil top is not always bounded above by the tropopause. The JC rises from the anvil top after the OT sinks.

2. Instruments and data

2.1 Observation

The observations were performed with six visible-light cameras mainly during the northern summer in 2016 when more cumulonimbus clouds tend to occur around Japan. Figure 2 shows the observation period, area, and the observed JC for each period. The methods to locate the JC and its distribution are discussed in Sections 3.1 and 4.1, respectively.

All the cameras and lenses used in this study are products of the Imaging Source Inc. (DMK24UJ003) and VS Technology Inc. (VS-1214H1), respectively. Table 1 shows the specifications of the camera and the lens. With those specifications, the angular resolution is about 7.5×10^{-3}° per pixel. At that resolution, the height of an object has about 10 m error when observed from 100 km away. For our observations, we used electronic shutters of the cameras as mechanical shutters are in general much more prone to mechanical damage for extended capture periods (such as in our case), due to a large number of individual images taken (open-close motions). Another merit of these cameras is the availability of computer software to control their behavior, such as the time-lapse rate (image frequency) and photographing period. The exposure was set automatically, with the maximum exposure length of 2 seconds, to adjust to the environmental lighting conditions. The aperture was always fully opened for nighttime observation. To control the sunlight intensity during the daytime, a special UV filter (TRANSHADE-BS-01 Gray, Tokuyama Corporation) was installed. The material of the filter can change its transparency depending on the UV exposure it receives. That is, when sunlight directly enters the lens during the daytime, the filter becomes darker, and overexposure is prevented. It is also useful for protecting the camera's sensors from excessive sunlight. To protect cameras from severe weather such as strong wind, low temperature, humidity and precipitation, cameras were set inside housing boxes.

The observatory at Mt. Fuji is accessible only in July and August. For that period, cameras were installed with two pairs of three cameras in two different locations (Fig. 2a): at the summit of Mt. Fuji and at the National Defense Academy (NDA) (Kanagawa, Japan). The distance between those two observation

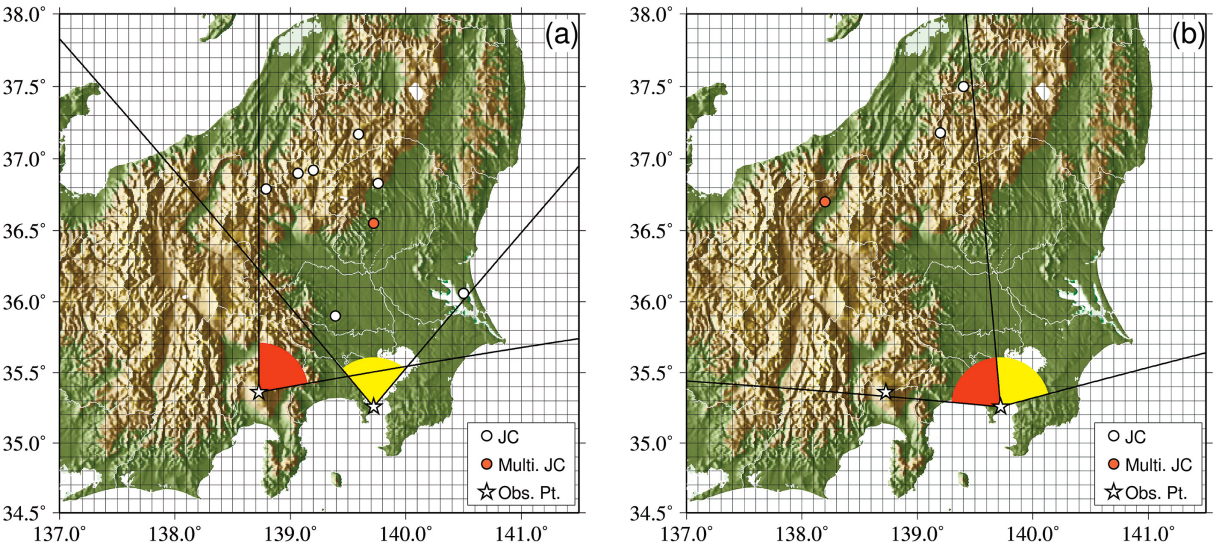

Fig. 2. Observation period, area, and observed jumping cirrus (JC) during the summer of 2016. (a) From July 12 to August 11, three cameras were set at the summit of Mt. Fuji (35.3°N, 138.7°E, 3,776 m above sea level (ASL)), and the other three at the National Defense Academy (NDA), Kanagawa, Japan (35.2°N, 139.7°E, 100 m ASL). (b) From August 19 to October 12, the observation was performed only at the NDA. The grid is longitude and latitude, and stars denote two different observation points. The coldest T_{bb} points of deep convective storms which generated the JC are plotted as circles. In particular, the two red circles denote where the multiple JC occurred during the same convective storm.

Table 1. The specifications of the camera and lens. The number in parentheses for the "Focal length" and "Angle of view" is the catalog specification to fit a normal camera with a 35 mm sensor.

Camera: DMK24UJ003 (Imaging Source Inc.)		Lens: VS-1214H1 (VS Technology Inc.)	
Definition	3856 × 2764 (10 MP)	Focal length	67 mm (12 mm)
Gradation	8 bit (black & white)	Angle of view	29 × 22 (59.9 × 44°)
Pixel size	1.67 × 1.67 μm	Distortion rate	−0.52 %

locations is ~90 km. The cameras' scopes at both locations were set so that they overlapped. If the same object is viewed from both places, the correct position of that object in latitude and longitude coordinates (as known as stereo analysis or the triangulation method) can be determined. During our observation, however, no convective storms were simultaneously detected from both places. Viewing at lower altitudes tends to be influenced by low-level clouds and hazy air in the mixed layer. Since the altitude of the summit of Mt. Fuji is 3,776 m above sea level (ASL), it is located in the free atmosphere, the view from Mt. Fuji is not interrupted, at least by nearby obstacles in the lower altitude, and thus, one can see farther than from lower places.

After the climbing season on Mt. Fuji finished, all the cameras were installed at the NDA, where they remained until early October (Fig. 2b). During that period, the scopes of the two cameras were not overlapped so that they could observe a wider area.

During the daytime (from 04:00 to 19:00 Japan standard time (JST) (Coordinated Universal Time (UTC) +9)), the cameras took a photograph every 15 seconds and every 60 seconds during nighttime (from 19:00 to 04:00 JST). The purpose of taking photographs at night is to obtain position information from the stars, such as the azimuth and elevation angles of each pixel of the photographs from the observation location (details are provided in Section 3.1). A 15-second time-lapse rate is optimal for obtaining sufficient quality, observing cloud motion, and reducing the total volume of the series of image data.

2.2 Detection of JC

The detection of JC is based on the relevant morphological facts described in previous studies (Wang et al. 2011). We used cases where the jumping motion was observed after the OT sank to the anvil. The shape of the JC after it jumps was not limited to the "sickle shape", as shown in Fig. 1 because the JC sometimes moved in depth, as seen from the cameras. On the other hand, we excluded the cirrus clouds that sank instantly in place after jumping instead of remaining above the anvil for a period of time. The other parameters, such as the wind shear, air temperature, and atmospheric instability, were not considered for the definition.

2.3 Analyzed data

All the satellite imagery in this study was obtained from Himawari-8, a geostationary meteorological satellite operated by the Japan Meteorological Agency (JMA) that has 16 spectral bands to observe the Earth and its atmosphere. In the area around Japan, the temporal resolution of the data is 2.5 min. For the detection of convective clouds, data from channel 3 and channel 13 are used in this study. Channel 3 is a visible band with a central wavelength of 0.64 μm and a horizontal resolution of 0.5 km at nadir. Channel 13 is a thermal IR band with a central wavelength of 10.4 μm and a horizontal resolution of 2 km at nadir. With this band, the temperature of the Earth's surface or the cloud top is detected as T_{bb}. In addition, channel 8, a water vapor absorption band with a central wavelength of 6.2 μm and a horizontal resolution of 2 km at nadir, was used to detect the water vapor layer and the T_{bb}.

To determine the environmental atmospheric conditions, we investigated the data—including the vertical profile of air temperature, wind speed, and wind direction—collected by a radiosonde that was launched twice a day at Tateno, Japan (36.05°N, 140.13°E).

Precipitation was also examined by using the radar network operated across Japan by the JMA, which has 20 sites all across Japan and whose band is 5 GHz frequency (C-band). We utilized the product of radar echo height and precipitation intensity estimated by the radar with grid point values. The former has a horizontal resolution of 2.5 km and vertical resolution of 2 km. The latter has a horizontal resolution of 1 km. Both are available every 10 min.

3. Methods

This chapter provides the methods of analyses, exemplifying a certain case as an example. The analyses were performed in the following order: (i) identify the distance, azimuth, and elevation angles of the JC from the observation point; (ii) calculate the spatial and temporal scales from the motion, distance, and angles; and (iii) examine the data collected from the radiosonde, radar, and satellites.

Figure 3 shows an example of the detected JC above a cumulonimbus (in several stages of its development), which occurred on August 4, 2016, near Tochigi, Japan, and was observed from the NDA. As in this example, a large cumulonimbus will typically occur in the evening hours during summer in Japan. A series of analyses for the case shown in Fig. 3 is demonstrated in this section. A summary of all of the results and discussion is provided in Section 4. As a supplement of this paper, the photographs for all JC cases and video footage for the JC cases of August 4, 2016 are available. The possible error sources in the following analyses are discussed in the appendix.

3.1 Identification of the location of the JC

Firstly, the elevation and azimuth angles from the cameras at each pixel in the photographs were determined by the stars. To scrutinize the position (azimuth and elevation angles) of the stars in the photographs, we used Stella Navigator Ver. 10 software (Astro Arts Inc., Japan). Using this software, the celestial sphere, including stars, planets, and the earth's topography on the horizon, is simulated for a specific date, time, and place. The errors caused by the atmospheric refraction are also included with this software (see the detail in appendix). Then, the real azimuth and elevation angles of the stars relative to the observation point can be determined in celestial coordinates (horizontal coordinates). At the same time, the positions of those stars in the photographs are given as x-y pixel numbers in the Cartesian coordinates on the photograph. By comparing those two pairs of values for more than 10 stars in the photographs, we can allocate azimuth and elevation angles to all the pixels in the photographs; hence, the direction of an arbitrary position in the photographs can be determined from the observation point.

Figure 3 shows an example of the photograph with the grid drawn based on the information of the azimuth and elevation angles of the pixels. At the time Figs. 3a and 3c were recorded, the two anvils were observed at 4.5° and 5.5° in elevation, respectively. The anvils were horizontally spread from −13° (left) to 11° (right) (the lower one) and from −5.8° to 3.8° (the higher one) in azimuth. The JC jumped in the direction of −3.5° azimuth and reached 6° of elevation with a width of 0.8° in azimuth.

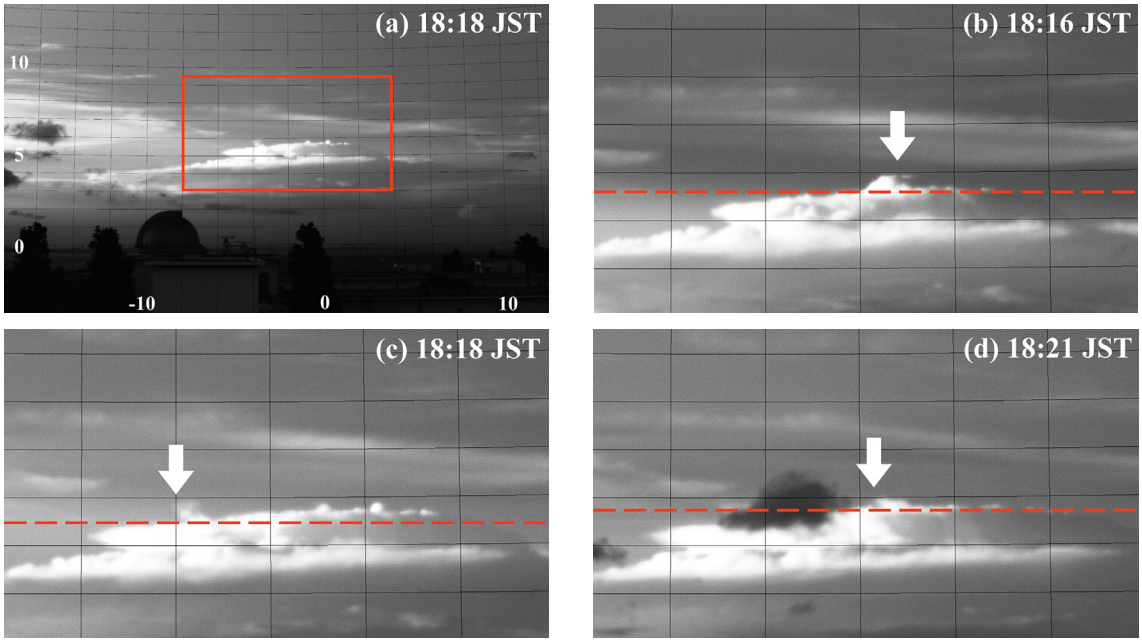

Fig. 3. Example of a time series of the jumping cirrus (JC) and the underlying convective storm from 18:16 to 18:21 JST (UTC +9) on August 4, 2016. It occurred near Tochigi, Japan (36.5°N, 139.7°E, 143.5 km from the NDA) and was observed from the NDA. For better visibility, the sharpness, brightness, and contrast of the images have been adjusted. Horizontal black lines denote the elevation angle by 1° increment. Vertical black lines denote the azimuth angle by 2° increments (see Section 3.1 for details). (a) The snapshot when the JC reached the highest altitude. The pictures of (b)–(d) correspond to the area bounded in red in (a), and a red, dashed line is drawn along the anvil top in (b)–(d). Note that the altitude of the anvil top varied slightly in (b)–(d) because of the lateral inclination and temporal variation. (b) An OT (denoted by the white arrow) rose up from the mature anvil top. (c) The first JC jumped upward from the anvil top, reached maximum height, and drifted westward (denoted by the white arrow). (d) The second JC (denoted by the white arrow) rose the right (east) side of the first one which was obscured by the black cloud closer to the observation site.

Secondly, to identify the location where the JC occurred, we utilized the IR T_{bb} image from the Himawari-8 channel 13 and calculated the distance between the observed JC and the observation point. Figure 4a shows an example of the IR T_{bb} image at 18:18 JST on August 4, 2016, which corresponds to the time of the photograph (Figs. 3a, c). In Fig. 4a, the area where the T_{bb} is more than 30 K lower than the ambient one is located in the direction of −3.5° in azimuth from the observation point (denoted as a white line), which is consistent with the azimuth of the photograph (Fig. 3a). Therefore, the anvil top of the convective cloud of the photograph is identified on the map in the latitude and longitude coordinates. To calibrate the parallax shift of the cloud top, we assumed 13 km height of top of cloud (which we call "satellite parallax" here; see the detail in appendix).

As shown in Fig. 3, the vertically two distinct tiers of anvil clouds also appear in Fig. 4a. It cannot be defined only in Fig. 3 whether there are two anvil clouds in a single storm or two separate anvil clouds along the line of the sight because the observation is from only one direction and the photograph is obscured. However, the former scenario is considered reasonable based on this IR T_{bb} image. The coldest T_{bb} value of the cloud top within the apparent spreading anvil area was 210 K, which is similar to the European case (Setvák et al. 2008).

In this second step, images from the Himawari-8 visible band are also inspected. Figure 4b shows an image from the visible band (channel 3) at the same time as Fig. 4a (Fig. 4c was used for other analysis in Section 3.4). The visible band of Himawari-8 has a high horizontal resolution (0.5 km at nadir), but it is still difficult (nearly impossible) to detect JC even at this higher spatial resolution. Moreover, especially in

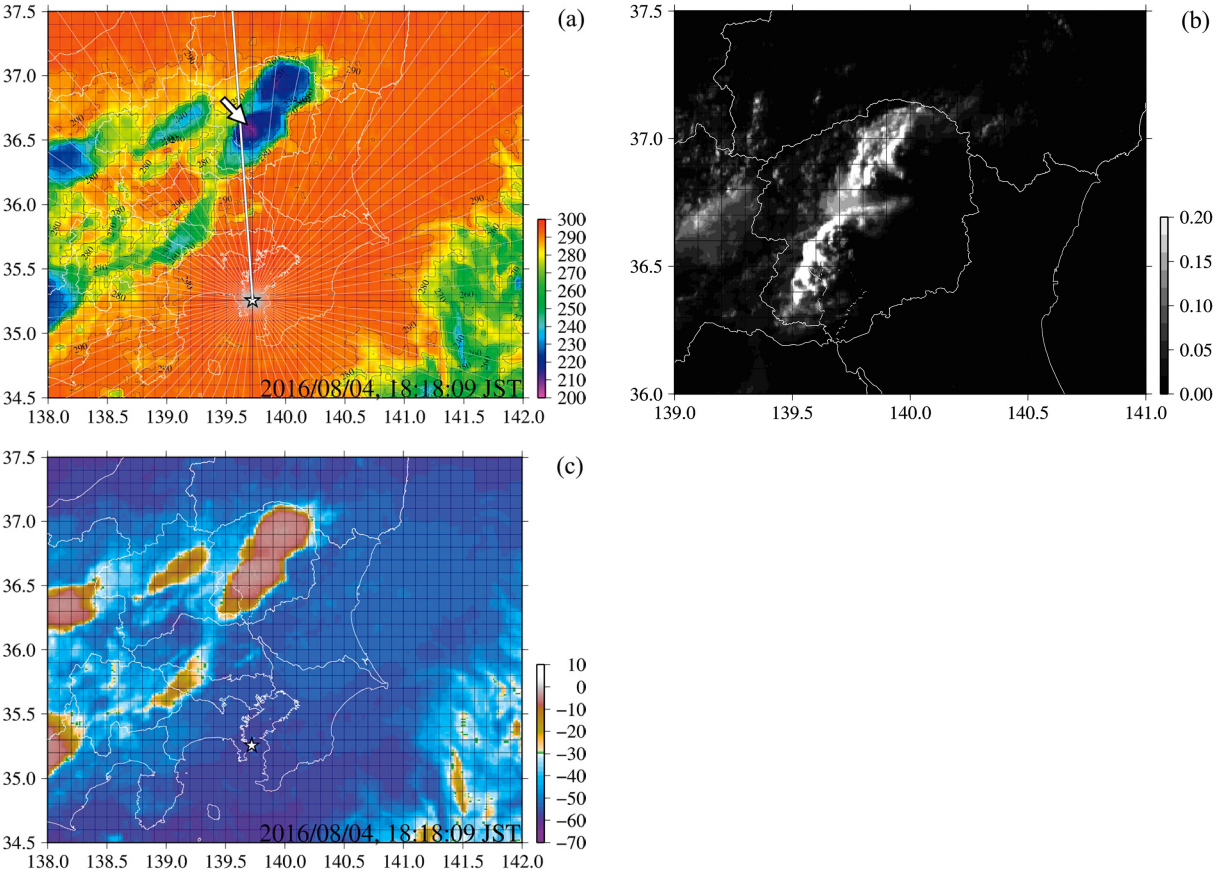

Fig. 4. Images from the Himawari-8 at 18:18 JST (UTC +9) on August 4, 2016. Black grid lines denote the latitude and longitude coordinates at 0.1° increments. White lines indicate coastlines and prefecture borders around the Kanto area in Japan. The star symbol depicts the observation point located at the NDA. (a) T_{bb} image from infrared (IR) band. The color bar denotes the value in K. The gray lines extending radially from the observation point denote azimuth angles in 5° increments. The white line and arrow denote the −3.5° azimuth line and the coldest T_{bb} point, respectively. (b) Visible-light image from channel 3. The grayscale stands for reflectivity, modified by solar illumination angle and tilt of the illuminated cloud. The brightest pixels represent highest, thick clouds, illuminated by the setting sun. The local sunset time of this day was 18:44 JST. (c) Distribution of brightness temperature difference, calculated by subtracting the T_{bb} of Himawari-8 channel 13 from the one of channel 8. The color bar denotes the value in K.

this case at around 18:00 JST (the time of sunset was 18:44 JST), the shape of the cloud top is seen only from the west side where the sunlight is shed from a lower altitude, as well as where the height gradient is large enough to cast a shadow dense enough to define the cloud top topography. Therefore, it is difficult to use the visible images from the satellite to detect JC and to explore its morphology. Additionally, the AACP was not found in this case.

The problem is that JC cannot be detected even by an IR T_{bb} image due to its small horizontal scale and lack of vertical profile of data. Also, stereo analysis was not applicable to this study, as mentioned in Section 2.1. Thus, we cannot determine the exact location of the JC. Alternatively, we regard the coldest point on the anvil top as the position of the JC and calculate the approximate distance from the observation point. As for the case shown in Fig. 4a, the coldest T_{bb} point is located 143.5 km from the observation point at 36.6°N, 139.7°E (denoted with an arrow). For the following analyses, we used this value as the JC distance.

There is another problem with determining the JC position, which we refer to as the “elevation parallax”, as shown in Fig. 5. When clouds are observed from

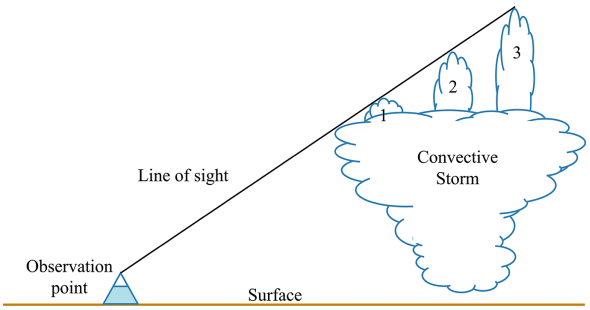

Fig. 5. Schematic diagram of the elevation parallax of jumping cirrus (JC). The solid black line denotes the observer's line of sight. In a two-dimensional picture, the appearance of the JC that occurred at the closest edge, the farthest edge, and between the two (1, 3, and 2, respectively) would be seen similarly due to the lack of perspective.

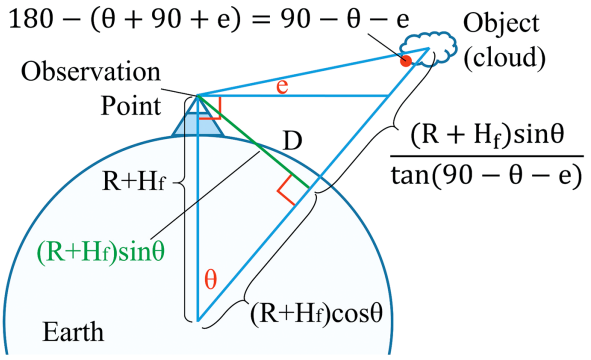

Fig. 6. Diagram of how to calculate the altitude of clouds. The distance on the surface is D, the elevation angle is e, and the cloud height is H_c. The height of the observation point is H_f, and the Earth's radius is R. The angle θ is the latitude difference between the observation point and the cloud location.

the ground levels, we cannot state the correct position of the JC along the line of sight due to a lack of perspective. To address this challenge, we calculated a range of distances between the front and rear edges of the anvil top seen from the observation point along the direction line identified in the photograph. By using this distance range, we were able to calculate the JC scale both for the case where the JC occurred at the front edge of the anvil (minimum height; denoted as "1" in Fig. 5) and for the case that occurred at the rear edge (maximum height; denoted as "3" in Fig. 5). The rear edge is not visible in the photographs. Thus, we empirically set the threshold of T_{bb} of 240 K as an anvil's edge outline in the IR images. Because the T_{bb} of the anvil top depends on the altitude, thresholds must be specific for each case to be strict. In this study, however, we consistently used the same threshold for all cases because we could not state the exact T_{bb} of the anvil top.

3.2 *Size and timescale*

Using the azimuth, elevation angles, and the distance between the clouds and cameras determined in Section 3.1, we can estimate the spatial scale of the cloud or the JC with a trigonometric function.

As per Fig. 6, the height of the cloud, H_c, can be determined using the following equation:

$$H_c = (R + H_f)\cos\theta + \frac{(R + H_f)\sin\theta}{\tan(90 - \theta - e)} - R, \qquad (1)$$

where R, H_f, and e are the Earth's radius (averaged as a spheroid, i.e., 6371 km), the height of the observation point, and the elevation angle, respectively. The angle θ can be approximated by

$$\theta = \frac{D}{R}, \qquad (2)$$

provided that $D \ll R$, where D is the distance between the observation point and the cloud. Note that all of the angles are degrees. In the case of Figs. 3a and 3c, the altitudes of the JC top, the higher anvil, and the lower anvil were 16.8 km, 15.6 km, and 13.0 km, which corresponds to elevation angles of 6.0°, 5.5°, and 4.5°, respectively. The jumping height, which is the difference between the altitude of the JC top and the higher anvil top, is therefore 1.3 km.

As in Fig. 7, the horizontal scale of the cloud, L_H, is roughly estimated by the following equation:

$$L_H \sim D\varphi, \qquad (3)$$

where the distance between the cloud and observation point is D, and the difference of azimuth angles between the left and right edge of the cloud from the observation point is φ, provided that φ is sufficiently small.

Next, the timescale of the JC is examined. Figure 3 exemplifies a portion of the lifetime of the cloud top appearance. In the time sequence, Figs. 3a and 3c are

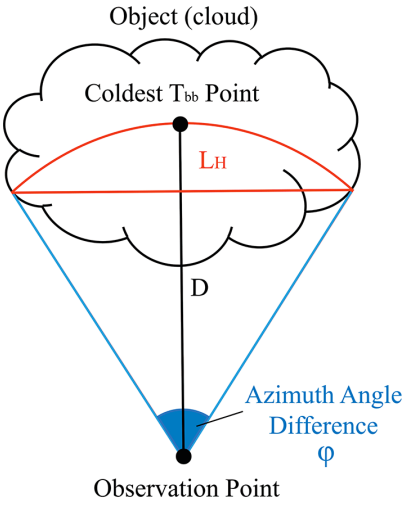

Fig. 7. Diagram of calculation of the horizontal scale of clouds as seen from above. The horizontal scale of a cloud, L_H, is numerically approximated by the arc length where the radius of the sector is the distance between the cloud and the observation point, D, and the difference of azimuth angles between the left and right edge of the cloud, φ.

snapshot of the moment when the first JC top reaches its highest altitude. Just before the first JC occurred, the OT rose up and sank in about 2 min on the right (east) side of the first JC (Fig. 3b). In Figs. 3a and 3c, it is confirmed that the first JC arose. Another JC occurred to the east (right) side of the first one before the first JC in Figs. 3a and 3c dissipated (Fig. 3d). Afterward, the underlying storm started decaying. The starting time of the first JC is 18:17 (not shown), just before it rose vertically from the higher anvil top (15.6 km; denoted by the red dashed line in Fig. 3c). In Figs. 3a and 3c, the first JC reached the maximum height of 16.84 km in about 80 s. Thus, by dividing the jumping height by this time, an average vertical speed of 15.9 m s^{-1} was determined. In this study, the duration of the JC was defined as the time from the start of the JC to the point when the JC becomes invisible. In this case, the first JC existed above the anvil until 18:30 (not shown); thus, the duration was approximately 13 min.

3.3 Environmental conditions

To investigate the relationship between the morphology of the JC and the physical variables of the environmental air, radiosonde, and ground radar data were examined. Figure 8 shows the vertical distribution of temperature, wind speed, and wind direction at 21:00 JST, August 4, Tateno, Japan. Compared with the JC in Fig. 3, the time and place are separated by approximately 3 h and 65 km, respectively.

The altitude of the tropopause was calculated from the radiosonde temperature profile following a definition by the World Meteorological Organization (WMO). We also employ the cold point tropopause (CPT), which is the altitude where the air temperature in the vertical profile is the lowest. According to the temperature profile of Fig. 8, the altitude of the WMO tropopause is 17.4 km (solid black line), and the CPT is 16.8 km (dashed black line) in this case. From the photograph in Figs. 3a and 3c, the altitude of the anvil is 15.6 km, which is different from both of the WMO tropopause and CPT. This may be because the radiosonde cannot necessarily show the right atmospheric conditions for the different time and locations. We estimate that the JC enters the stratosphere if the altitude of the JC surpasses either the WMO tropopause or the CPT. In this case, the JC reached 16.8 km as estimated by Eq. (1), which reached the CPT, and was then likely to enter the stratosphere. The T_{bb} of the coldest cloud top is 210 K (Fig. 4a), which is equivalent to an altitude of 15.1 km in the temperature profile (Fig. 8) and close to the anvil top height determined from the photograph. If the coldest T_{bb} denotes the OT, it would be lower than the T_{bb} of surrounding anvil top against this case. Therefore, the temperature profile from the radiosonde might not show the same value to the location of coldest cloud top.

The environmental wind speed and direction were also examined, as shown in Fig. 8. Homeyer et al. (2017) utilized objective analysis data for the horizontal wind profile instead of radiosonde and demonstrated that the storm-relative horizontal wind speed was mostly within the range of 5–25 m s^{-1} in the first 2–3 km above the tropopause in the case where the storm penetrated the tropopause. Because the storm-relative wind speed cannot be determined in this study, we set the layer of the jumping height to calculate the environmental wind shear magnitude. In Fig. 8, wind shear is −1.2 m s^{-1} km^{-1} for altitudes between 15.6 and 16.8 km. Above the anvil, at the altitude of 15.6 km, wind direction is predominantly easterly, and the camera photos show that the JC drifts westward, following that wind direction as it moves away from the overshooting point.

The value of the CAPE is also available from the radiosonde data. Using this, the potential updraft strength of storms was examined.

The ground precipitation radar data were examined

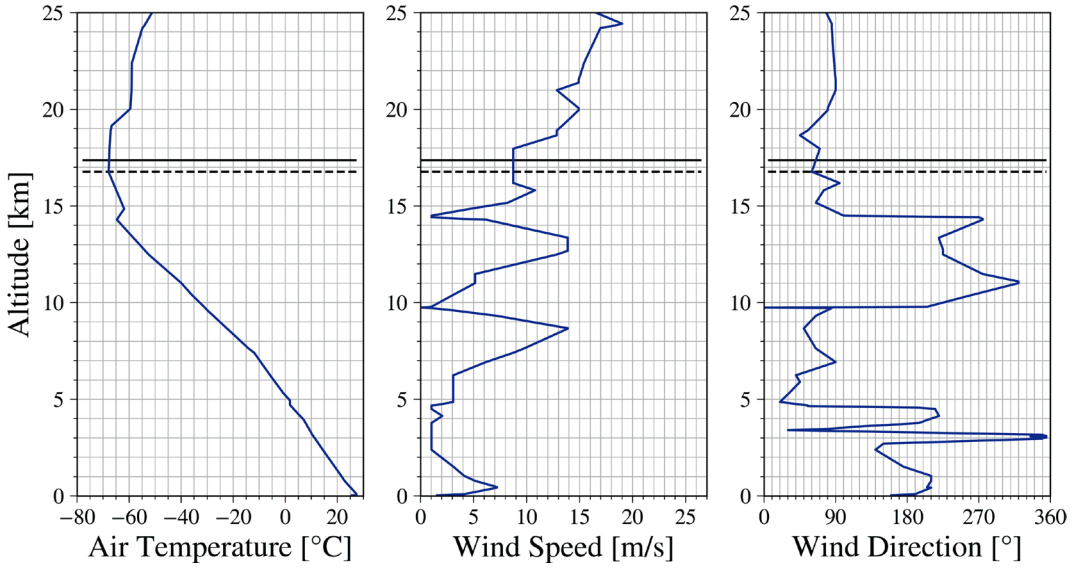

Fig. 8. Vertical profiles of air temperature, wind speed, and wind direction from a radiosonde at 21:00 JST (UTC +9), August 4, 2016, near Tateno, Japan. In each profile, the solid black line and the dashed black line denote the altitude of the tropopause based on the World Meteorological Organization's (WMO's) definition, 17.4 km, and the CPT, 16.7 km, respectively.

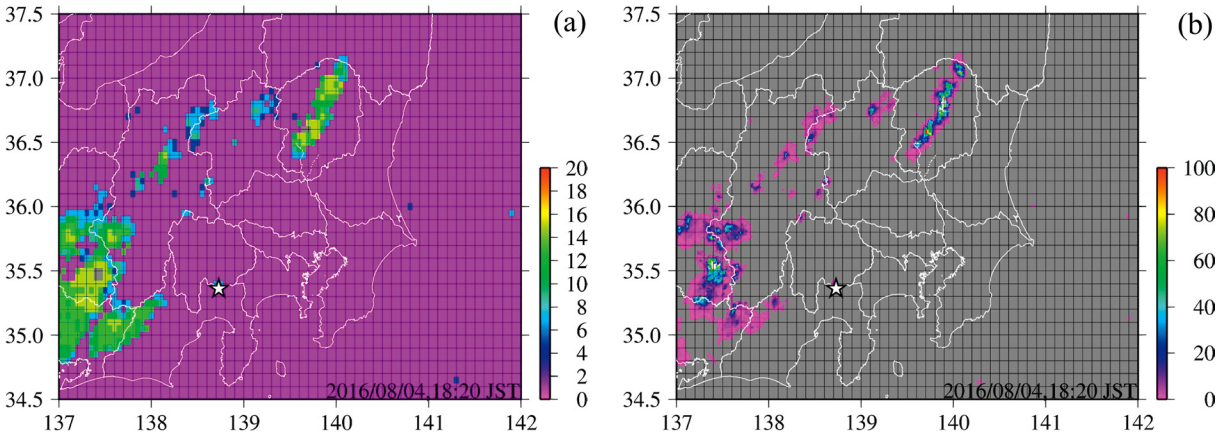

Fig. 9. (a) Radar echo height and (b) Estimated precipitation intensity at 18:20:44 JST (UTC +9) on August 4, 2016. The x-y labels are longitude-latitude coordinates, and the star in the center depicts the observation point, the National Defense Academy (NDA). The color bar denotes (a) the echo height in km and (b) the rain rate in mm h^{-1}.

for further analysis of the convection characteristics. Figure 9 shows (a) the radar echo height of the top of the convective core and (b) the radar-analyzed precipitation intensity. In Fig. 9, the strong radar echo and heavy rainfall is detected in the same area as where the convective storm is detected by the satellite images (Figs. 4a, b). Within that convective cloud, the maximum value of the radar echo is at the height of approximately 16 km (yellow color in Fig. 9a), which is consistent with the calculated altitude of the anvil (15.5 km). The precipitation intensity caused by the convective storms with the JC was examined to inspect the severity of the convection generating the JC. In Fig. 9b, with a horizontal resolution of 1 km,

the area with a strong precipitation intensity of more than 100 mm h^{-1} is denoted with red dots and located near the coldest T_{bb} point of Fig. 4a. The maximum precipitation intensity is 203 mm h^{-1} within the same convective cloud.

3.4 Water vapor above deep convection

Figure 4c shows the distribution of the BTD values. A positive value was not detected above these convective storms, most likely because the temperature gradient above tropopause was negligible, which would prevent positive BTD values to be detected even if the humidity above the anvil top was sufficient.

4. Results and discussion

This chapter shows the results and relevant discussions from the above analyses for all the cases. In total, we found 14 JC cases: 6 from the summit of Mt. Fuji and 8 from the NDA. The results include (1) the altitude of the anvil top and the JC top, the horizontal scale of the anvil, and the width of the JC, which are all calculated based on the photographs; (2) the timescale from the time-lapse movie; (3) the vertical speed calculated from (1) and (2); (4) the cloud top temperature from Himawari-8 channel 13; (5) the BTD from Himawari-8 channels 8 and 13; (6) the altitude of the tropopause, vertical wind shear, and value of CAPE from the radiosonde; and (7) the echo height of convective core and precipitation intensity from the radar. Table 2 shows the terminology for those resulted values and Table 3 shows the results of (1)–(7) for all the cases.

4.1 Distribution of the JC

Figure 2 shows the 14 points with the coldest T_{bb} in the convective cloud, which was accompanied by the JC. It should be noted that JC must be generated more frequently than we observed because the camera's sight was often interrupted by the local fog, rain, and low-level clouds that frequently occur when cumu-

Table 2. List of investigated values.

Calculated/observed value	Description
Anvil Top	Altitude of anvil top calculated by the elevation angle from the photograph and the distance to the coldest T_{bb} point from Himawari-8 channel 13 (10.4 μm in wavelength)
Echo Height	Altitude of radar echo height top observed by the C-band radar of JMA
JC Top	The same as anvil top but altitude of the JC top
Front Height	Altitude of the JC top calculated by the elevation angle from the photograph and the distance to the front edge (240 K outline) of anvil from Himawari-8 channel 13
Rear Height	The same as front height but the distance to the rear edge
Jumping Height	Difference between the anvil top and the JC top above
Horizontal Scale of Anvil	Horizontal scale of anvil calculated by the azimuth angle from the photograph and the distance to the coldest T_{bb} point from Himawari-8 channel 13
Width	The same as horizontal scale of anvil but horizontal scale of the JC
Vertical Jumping Speed	Division of the jumping height by the time from when the JC jumps to when the JC reaches its maximum height
Duration	Time until the JC disappears from the view of the visible-light camera
Cloud Top IR T_{bb}	The lowest T_{bb} value on the cloud top observed by Himawari-8 channel 13
BTD	Subtraction of the T_{bb} value by Himawari-8 channel 13 from the one by channel 8 (6.2 μm in wavelength)
CAPE	Observed value by the radiosonde
CPT	Altitude of the coldest air temperature in the vertical profile observed by the radiosonde
WMO	Altitude of tropopause based on the definition by WMO using the vertical profile of air temperature observed by the radiosonde
Vertical Wind Shear	Subtraction of the wind speed at the altitude of anvil top from the one at the JC top using the vertical profile of wind observed by the radiosonde
Precip. Intensity	Precipitation intensity estimated by the radar echo observed by the C-band radar of JMA

Table 3. Resulting quantities from observation and calculation for all 14 jumping cirrus (JC) cases. For each instance in a row, the anvil, the JC, and the atmospheric conditions are listed in columns. The definition of value in each column is described in Table 2. The row with bold fonts is the case described in Section 3, the hyphen denotes no value, and the bottom two rows contain the average and standard deviation (SD) value.

Case No.	Date	Time	Location		Anvil				Jumping Cirrus							Atmospheric Condition					
					Altitude [km]		Cloud Top IR T_{bb} [K]	Horizontal Scale [km]	Altitude [km]			Width [km]	Jumping Height [km]	Vertical Jumping Speed [m s^{-1}]	Duration [s]	Tropopause		Vertical Wind Shear [m s^{-1} km^{-1}]	CAPE [J kg^{-1}]	Precip. Intensity [mm h^{-1}]	BTD [K]
					Anvil Top	Echo Height			JC Top	Front Height	Rear Height					CPT [km]	WMO [km]				
1	7/29/2016	16:35:58	Naeba, Niigata	36.79°N 138.79°E	12.7	15.0	230	17.2	14.9	14.1	15.0	3.1	2.2	5.1	810	16.9	17.4	0.5	0.0	146.5	−8
2	7/30/2016	13:15:01	Okutone Lake, Gunma	36.90°N 139.07°E	11.6	13.0	235	22.4	12.8	12.7	13.0	1.2	1.2	8.1	450	16.4	17.0	4.3	0.0	144.5	−10
3	7/30/2016	14:22:37	Osegahara, Gunma	36.92°N 139.20°E	12.5	15.0	230	25.5	14.1	13.7	14.4	1.2	1.6	6.5	555	16.4	17.0	−0.5	0.0	168.5	−7
4	7/30/2016	14:28:23	Nanagatake, Fukushima	37.17°N 139.59°E	13.1	15.0	230	25.9	15.0	14.0	15.1	1.5	1.9	4.9	1575	16.4	17.0	−3.4	0.0	203.0	−7
5	7/31/2016	12:28:11	Kasumigaura, Ibaraki	36.06°N 140.50°E	11.9	13.0	235	19.9	12.8	12.5	13.5	1.9	0.9	5.3	839	16.0	16.3	0.8	69.0	23.5	−7
6	8/2/2016	10:46:19	Nikko, Tochigi	36.83°N 139.76°E	13.8	15.0	225	16.4	14.8	14.5	15.0	1.6	1.0	5.1	–	16.7	16.8	−8.1	1124.0	185.0	−10
7	8/4/2016	16:07:20	Sayama, Saitama	35.90°N 139.39°E	13.6	15.0	220	25.0	14.5	13.2	15.7	1.4	1.0	11.0	671	16.8	17.4	−10.2	782.3	142.5	−7
8	**8/4/2016**	**18:18:23**	**Kanuma, Tochigi**	**36.55°N 139.72°E**	**15.6**	**15.0**	**210**	**59.7**	**16.8**	**14.8**	**18.8**	**2.0**	**1.3**	**15.9**	**782**	**16.8**	**17.4**	**−1.2**	**782.3**	**203.0**	**−2.5**
9	8/4/2016	18:21:04	Kanuma, Tochigi	36.55°N 139.72°E	16.3	15.0	210	59.7	16.8	14.8	18.8	1.5	0.5	2.8	292	16.8	17.4	0	782.3	203.0	−2.5
10	8/21/2016	16:28:24	Nagano, Nagano	36.70°N 138.20°E	14.7	15.0	220	37.5	16.5	15.2	17.2	1.8	1.9	12.3	316	18.7	17.0	−1.1	1384.0	154.5	−6
11	8/21/2016	16:37:11	Nagano, Nagano	36.70°N 138.20°E	13.9	15.0	220	42.6	15.4	14.0	16.5	1.8	1.5	10.9	346	18.7	17.0	2.7	1384.0	161.5	−6
12	8/21/2016	17:07:59	Nagano, Nagano	36.70°N 138.20°E	13.6	15.0	225	49.2	14.3	13.9	14.7	1.1	0.8	5.5	706	18.7	17.0	−2.7	1384.0	98.5	−6
13	8/21/2016	17:29:52	Oonuma, Fukushima	37.50°N 139.40°E	16.0	15.0	220	24.9	17.8	16.5	19.3	0.9	1.8	14.8	345	18.7	17.0	0.1	1384.0	76.5	−7
14	8/21/2016	17:33:38	Arasawadake, Niigata	37.18°N 139.20°E	14.2	15.0	220	18.3	15.3	14.6	15.6	1.9	1.2	4.2	646	18.7	17.0	3.7	1384.0	76.5	−7
Average					13.8	14.7	224	31.7	15.1	14.2	15.9	1.6	1.3	8.0	641	17.3	16.9	−1.1	747.1	141.9	−7
Standard Deviation					1.4	0.7	7.7	14.7	1.4	1.0	1.9	0.5	0.5	4.0	329	1.1	0.3	3.9	589.6	52.6	2.1

lonimbus clouds occur. The JC occurrence points tended to correspond with the mountainside, which is reasonable for the cumulonimbus occurrence by the forcible rising of the air. It is worthwhile to note that the multiple JC occurred from one convective cloud in two cases: one at 36.55°N, 139.72°E (Case No. 7 and 8 in Table 3) and the other at 36.7°N, 138.2°E (Case No. 10, 11, and 12 in Table 3). The former is equivalent to the Figs. 3a, 3c, and 3d. Also, more JC was observed for the period of Fig. 2a than Fig. 2b.

4.2 Averaged characteristics of the JC

The averaged value and standard deviation (SD) in parentheses are shown as follows. The calculated anvil top and the JC top were 13.8 (1.4) km and 15.1 (1.4) km, respectively, and hence the jumping height was 1.3 (0.5) km. The JC's width was 1.6 (0.5) km, and the vertical jumping speed was 8.0 (4.0) m s^{-1}. However, when the elevation parallax is considered, the JC top altitude had a range from 14.2 (1.0) km to 15.9 (1.9) km as possibilities for the cases where the JC occur at the front and rear edge of the anvil. Based on the photographs, the JC remained atop the anvil for about 11 min. These values of the jumping height, the altitude of the JC top, vertical jumping speed, and duration are similar to the ones simulated by the numerical model by Wang et al. (2011). Only the horizontal scale (width) of the JC was significantly smaller than the simulation result of 5–15 km. It should be noted that the JC is visualized by the spatial distribution of humidity in the model simulation (Wang et al. 2011), which affects the difference of the size of the JC. Moreover, we could only look at a single side of the JC in our observations, whereas we can see the arbitrary side in the model. Thus, our result did not necessarily show the maximum size of the JC. The direction of flow of the JC was along the environmental wind in 4 of the 14 cases.

As for the underlying anvil, the radar echo height that shows the maximum height of the convection, visualized by precipitation particles, was 14.7 km, 0.9 km higher than the anvil top altitude calculated from cameras. This is because the cameras and radar observe different size of cloud particles; the former can observe relatively smaller cloud particles and the latter observes larger ones. Also, calculated anvil top represents the altitude of the front edge of the anvil, whereas the echo height is the highest value of that convective cloud. For all of the cases, the altitude of the coldest IR T_{bb} estimated from the temperature profile of the radiosonde was lower than that of the anvil top height calculated from camera photographs (not shown). The anvil top height, determined both from the photographs and the coldest IR T_{bb}, was lower than the CPT and WMO tropopause for all of the cases. Thus, the anvil top most likely has not reached the tropopause.

However, the JC top reached the WMO tropopause in 1 of 14 cases (at 17:29 JST on August 21) and reached the CPT in 2 of 14 cases (at 18:18 and 18:21 JST on August 4), which implies the possibility of the JC's protrusion into the LS. On the other hand, the BTD value was negative for all of the cases, and no evidence of hydration of the LS by the JC was detected. In our most cases, the JC did not penetrate the tropopause. Therefore, even if the JC moistened the layer above the anvil top, that layer was not the LS which is warmer than UT, and thus BTD value was not positive. It is important that in most of our cases, the JC occurred under the tropopause, and thus JC itself does not directly imply moistening of the LS.

The averaged and maximum value of estimated precipitation was 141.9 mm h^{-1} and 203.0 mm h^{-1}, respectively, which were the instantaneous values around the time of the JC occurrence. These values show the strong severity of the underlying thunderstorms. Except for 1 case where the instantaneous maximum value of precipitation was only 23.5 mm h^{-1}, the cumulonimbus causing the JC was accompanied by heavy rain. We do not mention the value of precipitation specific to the storms with JC since we do not have plenty of data of precipitation of storms without JC.

Figure 10 shows the frequency distribution of "jumping height", "width", "vertical jumping speed", and "duration". The mode is 0.5–1.0 km, 1.0–2.0 km, 5.0–7.5 m s^{-1}, and 10–15 min, respectively. The median is 1.3 km, 1.6 km, 6.0 m s^{-1}, and 646 s, respectively. As it shows, the parameters about the JC vary with cases. To investigate what brings these variations, we also calculated the correlation between all parameters. However, no results showed a strong correlation between any two parameters. It means the scale of JC is not related to the CAPE, anvil size, precipitation, and environmental wind shear. We must note that as for the wind shear, storm-relative wind may be more appropriate to inspect the correlation to the JC.

We also checked the time variation of the maximum echo height and precipitation intensity within the cloud from radar, and the coldest T_{bb} from Himawari-8. However, remarkable changes were not found before and after the JC occurred.

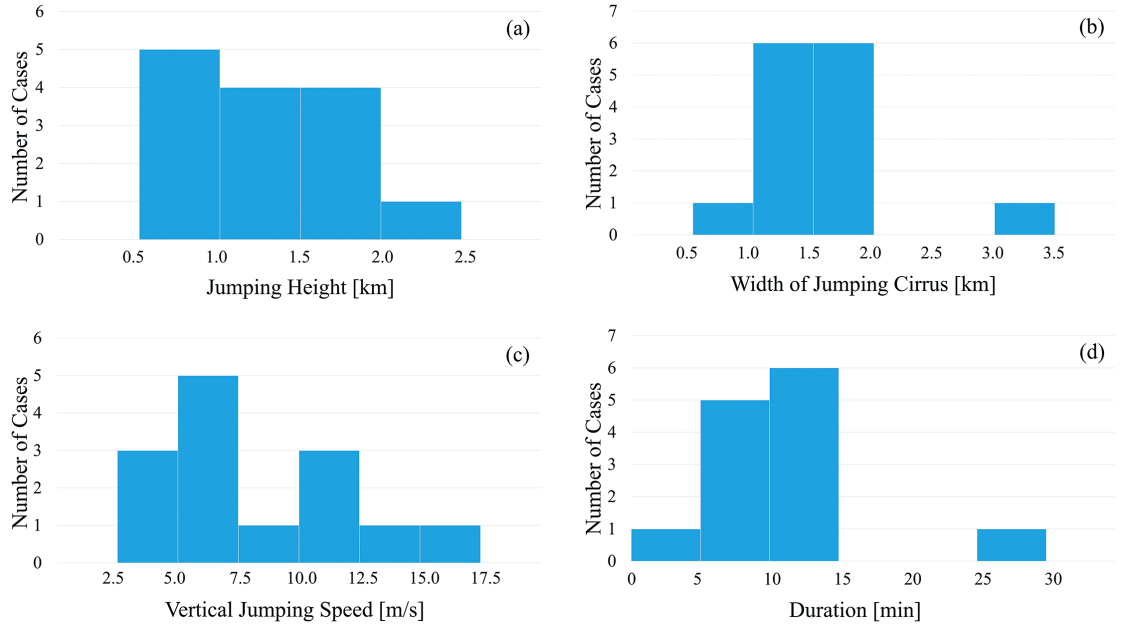

Fig. 10. Frequency distribution of the spatial and temporal scale of the JC. The vertical axis contains the number of cases, and the horizontal axis is the range of (a) jumping height in km, (b) width in km, (c) vertical jumping speed in m s^{-1}, and (d) duration in min.

4.3 Difference from the previous studies

The magnitude of the convective storms around Japan investigated in this study is much weaker than the previous numerical JC studies of severe thunderstorms in the United States of America (USA). The horizontal scale of the underlying anvil was less than 60 km in our cases, whereas it was more than 300 km in the USA case (Homeyer et al. 2017). One of the reasons for this difference is that the USA cases in their study were mainly supercell thunderstorms, whereas our cases were relatively short-lived single cell storms. JC could occur in both types of storms, whereas AACPs tend to form above the more severe storms like supercells.

In terms of the CAPE, our JC cases have values of less than 1384 J kg^{-1}, being 747.1 J kg^{-1} on average, whereas some cases had a zero value. These values are consistent with the most frequent value of CAPE (1000–1500 J kg^{-1}) for the cases of convective storms causing heavy rainfall around Tokyo, Japan (Fig. 16 by Fujibe et al. 2002). On the other hand, the typical value of CAPE for the severe thunderstorm cases is larger in the USA (~ 2000 J kg^{-1} in Table 3 by Bluestein and Jain 1985), whereas the JC case by Wang (2003) has over 3000 J kg^{-1}. However, as this study shows, even weaker convection can cause JC.

Another difference from the previous studies about JC is the wind shear. One possible mechanism to cause a cross-tropopause protrusion like JC is a diabatic gravity wave breaking on the top of the anvil. The previous studies utilizing cloud numerical models succeeded in reproducing the JC caused by gravity wave breaking, though its direct observation is difficult. Some previous studies demonstrate that strong wind shear in the UTLS is an important characteristic for the gravity wave breaking (see Section 1). In this study, averaged wind shear is calculated for the layer of the jumping height, which lies in the UTLS (actually in the UT for most of our cases) because the anvil did not reach the tropopause in all the cases. Its average value of all 14 cases is −1.1 m s^{-1} km^{-1}. The value is smaller than the previous studies (Homeyer et al. 2017). To compare more appropriately, we require data of storm-relative wind, not environmental wind. The wind speed in the LS is faster than the one in the UT for the 6 cases similar to Fig. 8.

For all of our cases, the JC and the AACP were undetectable by both the visible and infrared imagery from the satellite. Compared with the cases in previous studies where the AACP was detected, the smaller wind shear above the anvil and the smaller horizontal scale of the JC and the convective clouds are specific

to our cases; this stands in contrast to the similarity of the vertical scale of the JC. Therefore, the large wind shear seems to be important to the formation of an elongated JC with a large length. However, the relationship between the creation of JC and AACPs and the magnitude of the underlying convection and wind shear is uncertain because we could not detect an AACP. We should be more cautious to infer that JC can create an AACP in the LS because JC does not always protrude into the LS as our results showed.

5. Summary and conclusion

In this study, ground-based observation using six cameras was performed to study the JC's characteristics, and its advantage that we can observe vertical and consecutive change of JC was demonstrated. During the summer, when the atmospheric conditions are favorable for the generation of deep convections in Japan, 14 JC cases were observed in total. The motion of the JC material was different from case to case.

Quantitative analyses of the JC revealed that the size of the JC was 1.3 (SD = 0.5) km high and 1.6 (SD = 0.5) km wide, and it reached an altitude of 15.1 (SD = 1.4) km on average. The JC rose at a vertical jumping speed of 8.0 (SD = 4.0) m s^{-1}, and it took about 11 (SD = 5.5) min until it disappeared above the anvil through sublimation into water vapor and sedimentation down to the anvil. The time-lapse movies illustrated that the JC transported cloud particles atop the anvil clouds. Evidence of the increase of water vapor in the LS was not documented using the BTD method. However, the calculated altitudes of the tropopause and the JC top implied that 3 JC cases were likely to enter the stratosphere.

As for the ambient atmospheric conditions, the wind shear for the jumping height was -1.1 m s^{-1} km^{-1} on average. In half of the cases, the wind was stronger with an altitude above the anvil top, which indicates positive wind shear.

The new finding in this study is that all the characteristics mentioned above are generally consistent with previous studies, such as the results from the numerical model simulations, but the primary differences are the horizontal scale of the JC, the magnitude or severity of the underlying convective storms causing the JC, and wind shear on the anvil top. Particularly, the JC in this study occurred even from evidently weaker convection as compared to severe thunderstorms in the USA.

There is still uncertainty in the relationship between the scale (height, duration, and speed), occurrence, and frequency of the JC, and the intensity of the underlying convective storms.

For future work, the estimation of the amount of water vapor transported into the stratosphere via one JC event, based on observations, is highly desirable. In addition, global observations of JC phenomena are required for better understanding of the locally typical characteristics of JC, as the magnitude of convective storms may exhibit significant variations even in areas at the same latitude. This study has demonstrated that observations of JC using ground-based cameras are effective. They lead to a better understanding of JC characteristics and their impacts on the climate system.

Acknowledgments

This work was supported in part by the Collaborative Research Program of Research Institute for Applied Mechanics, Kyushu University, and JSPS Kakenhi JP17H06139. The observation at Mt. Fuji was performed at the Mt. Fuji Weather Station, which is currently managed by the Mount Fuji Research Station (MFRS), a nonprofit organization certified by the government of Japan. They helped to support our work, including the installation and maintenance of the cameras. The data from Himawari-8 were obtained from the NICT Science Cloud at National Institute of Information and Communications Technology. The radiosonde data were obtained from the Department of Atmospheric Science, University of Wyoming (http://weather.uwyo.edu/upperair/sounding.html). The precipitation data were collected and distributed by the Research Institute for Sustainable Humanosphere, Kyoto University (http://database.rish.kyoto-u.ac.jp/index-e.html).

Appendix: Evaluation of Errors

There are possible errors in each analysis. Those errors mainly stem from the observation angles and distances, with the latter being more dominant.

The angle errors induced by the information about the stars from the Stella Navigator are negligible because the software has precision within an error of 0.1 s of arc. This means that there is only 1 m of height error at a distance of 100 km. The software also corrects the error caused by the atmospheric refraction and the aberration of the light when observing farther objects such as stars. The impact of the atmospheric refraction is small (about 0.1 degree error) in about 1–5 degree elevations within which the photographs of cumulonimbus were taken in most of our cases.

The angle errors from the camera are also small. With the spec of the camera used in this study, 1 pixel

has the angular resolution of about 7.5×10^{-3} degree. That is equivalent to 10 m in height at a distance of 100 km, which is small enough to measure the height of convective cloud. The distortion rate of the camera and the misalignment of the stars' information in the photograph cause a few pixels gap, resulting in a height error of tens of meters at a distance of 100 km.

To verify the calculation method of this study, we calculated the height of Mt. Fuji observed at the NDA using the camera and obtained a height of 3.77 km, close to the true value (3.776 km). This verification step demonstrated that the distance between Mt. Fuji and the NDA was correctly fixed; and thus, the source of error must be the angles. Note that the clouds observed by cameras have relatively fuzzy shape and indecisive edge as compared to the stars and Mt. Fuji which have discrete shape and well-defined edge. Therefore, there is also uncertainty of angles when retrieving the position of clouds from photographs.

The error caused by the distance between the clouds and the cameras is relatively large in this study. For example, if a cloud is observed at an elevation of 3°, the height changes 50 m with a 1 km difference in the distance. One of the points where the distance errors occurred is the determination of the location of the JC, as mentioned in Section 3.1. Another is the parallax correction of the Himawari-8 data (Fig. 1 by Iwasaki et al. 2015). In this study, the satellite-based parallax correction was applied assuming the cloud top height to be 13 km.

Supplements

Supplement 1 shows the photographs of all 14 cases, which are at original size, but their contrast, brightness, and sharpness are adjusted (enhanced) for better visibility.

Supplement 2 is the same to Supplement 1, except that the photographs are cropped and magnified, centering these at the jumping cirrus.

Supplement 3 is a time-lapse video, showing the evolution and motion of jumping cirrus of the case on August 4, 2016, which corresponds to Section 3 (Case No. 8 and 9 in Table 3).

Supplement 4 is the same, for Case No. 7 in Table 3.

References

Bedka, K., E. M. Murillo, C. R. Homeyer, B. Scarino, and H. Mersiovsky, 2018: The above-anvil cirrus plume: An important severe weather indicator in visible and infrared satellite imagery. *Wea. Forecasting*, **33**, 1159–1181.

Bluestein, H. B., and M. H. Jain, 1985: Formation of mesoscale lines of precipitation: Severe squall lines in Oklahoma during the spring. *J. Atmos. Sci.*, **42**, 1711–1732.

Danielsen, E. F., 1993: In situ evidence of rapid, vertical, irreversible transport of lower tropospheric air into the lower tropical stratosphere by convective cloud turrets and by larger-scale upwelling in tropical cyclones. *J. Geophys. Res.*, **98**, 8665–8681.

Fujibe, F., K. Sakagami, K. Chubachi, and K. Yamashita, 2002: Surface wind patterns preceding short-time heavy rainfall in Tokyo in the afternoon of midsummer days. *Tenki*, **49**, 395–405 (in Japanese with English abstract).

Fujita, T. T., 1974: *Overshooting thunderheads observed from ATS and Learjet. Satellite and Mesometeorology Research Project*. SMR Research Paper No. 117, Department of the Geophysical Sciences, The University of Chicago, 29 pp.

Fujita, T. T., 1982: Principle of stereoscopic height computations and their applications to stratospheric cirrus over severe thunderstorms. *J. Meteor. Soc. Japan*, **60**, 355–368.

Hassim, M. E. E., and T. P. Lane, 2010: A model study on the influence of overshooting convection on TTL water vapour. *Atmos. Chem. Phys.*, **10**, 9833–9849.

Homeyer, C. R., J. D. McAuliffe, and K. M. Bedka, 2017: On the development of above-anvil cirrus plume in extratropical convection. *J. Atmos. Sci.*, **74**, 1617–1633.

Iwasaki, S., T. Shibata, J. Nakamoto, H. Okamoto, H. Ishimoto, and H. Kubota, 2010: Characteristics of deep convection measured by using the A-train constellation. *J. Geophys. Res.*, **115**, D06207, doi:10.1029/2009JD013000.

Iwasaki, S., Z. J. Luo, H. Kubota, T. Shibata, H. Okamoto, and H. Ishimoto, 2015: Characteristics of cirrus clouds in the tropical lower stratosphere. *Atmos. Res.*, **164–165**, 358–368.

Levizzani, V., and M. Setvák, 1996: Multispectral, high-resolution satellite observations of plume on top of convective storms. *J. Atmos. Sci.*, **53**, 361–369.

Nielsen, J. K., N. Larsen, F. Cairo, G. Di Donfrancesco, J. M. Rosen, G. Durry, G. Held, and J. P. Pommereau, 2007: Solid particles in the tropical lowest stratosphere. *Atmos. Chem. Phys.*, **7**, 685–695.

Sang, W., Q. Huang, W. Tian, J. S. Wright, J. Zhang, H. Tian, J. Luo, D. Hu, and Y. Han, 2018: A large eddy model study on the effect of overshooting convection on lower stratospheric water vapor. *J. Geophys. Res.*, **123**, 10023–10036.

Schmetz, J., S. A. Tjemkes, M. Gube, and L. van de Berg, 1997: Monitoring deep convection and convective overshooting with METEOSAT. *Adv. Space Res.*, **19**, 433–441.

Setvák, M., and C. A. Doswell III, 1991: The AVHRR channel 3 cloud top reflectivity of convective storms. *Mon.*

Wea. Rev., **119**, 841–847.

Setvák, M., D. T. Lindsey, R. M. Rabin, P. K. Wang, and A. Demeterová, 2008: Indication of water vapor transport into the lower stratosphere above midlatitude convective storms: Meteosat Second Generation satellite observations and radiative transfer model simulations. *Atmos. Res.*, **89**, 170–180.

Solomon, S., K. H. Rosenlof, R. W. Portmann, J. S. Daniel, S. M. Davis, T. J. Sanford, and G.-K. Plattner, 2010: Contributions of stratospheric water vapor to decadal changes in the rate of global warming. *Science*, **327**, 1219–1223.

Wang, P. K., 2003: Moisture plumes above thunderstorm anvils and their contributions to cross-tropopause-transport of water vapor in midlatitudes. *J. Geophys. Res.*, **108**, 4194, doi:10.1029/2002JD002581.

Wang, P. K., 2004: A cloud model interpretation of jumping cirrus above storm top. *Geophys. Res. Lett.*, **31**, L18106, doi:10.1029/2004GL020787.

Wang, P. K., M. Setvák, W. Lyons, W. Schmid, and H.-M. Lin, 2009: Further evidences of deep convective vertical transport of water vapor through the tropopause. *Atmos. Res.*, **94**, 400–408.

Wang, P. K., S.-H. Su, Z. Charvát, J. Št'ástka, and H.-M. Lin, 2011: Cross tropopause transport of water by mid-latitude deep convective storms: A review. *Terr. Atmos. Oceanic Sci.*, **22**, 447–462.